

Supporting Information

Plasmonic Nanobowtie-fluidic Device for Sensitive Detection of Extracellular Vesicles by Raman Spectrometry

Mahsa Jalali,^a Sayed Imman Isac Hosseini,^a Tamer AbdelFatah,^a Laura Montermini,^b Sebastian Wachsmann Hogiu,^a Janusz Rak,^b Sara Mahshid*^a

^a. Department of Bioengineering, McGill University, Montreal, QC H3A 0E9, Canada

^b. Research Institute of the McGill University Health Centre (RIMUHC), Montreal, Quebec, Canada

* email: sara.mahshid@mcgill.ca

Fabrication:

Recent advances in amplifying the SERS spectrum using a variety of plasmonic nanostructures, including metallic nanoparticles¹⁻³, metallic bowl-patterns^{4,5}, nanohole arrays^{6,7} and *etc.*^{8,9} shed light on the potential of developing surpassed nanostructures for enhanced SERS detection of EVs. Here, a combined bottom-up and top-down approach was adopted to develop an array of plasmonic nanobowties standing on triangular-shaped metal-oxide to further enhance the plasmonic-assisted EM-field (**Figure S1a**). **Figure S1b** and **Figure S1c** shows the brightfield microscopy and SEM images of the closed-packed nanoparticles self-assembly pattern, respectively. The inset demonstrates the fabricated nanobowties after lift-off. The high-resolution images via fake-color demonstrate the nanobowties in cyan.

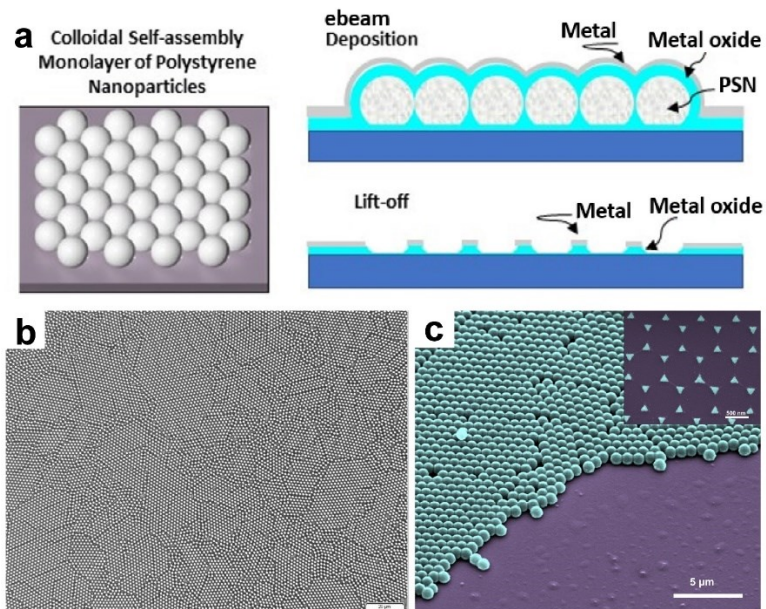


Figure S1. (a) Schematic illustration of fabrication method. (b) optical images of the self-assembly nanoparticles. (c) SEM image of the self-assembly nanoparticles and fabricated nanobowties platform after lift-off.

FDTD Simulation:

In general, Raman spectroscopy is an optical read-out system which translates the vibrational and rotational motions of chemical bonding structures into spectral peaks based on the recorded scattering of a coherent beam (laser) by the analyte. SERS amplifies subtle signal intensities based on strong EM fields generated in a plasmonic substrate⁹. **Figure S2a** demonstrates the apex, gap, materials, and boundary parameters used for simulations. The reflectance spectra of plasmonic nanobowties illuminated by a broad-band plane wave (**Figure S2b**) demonstrates the gap-dependent plasmonic light absorption pattern. The EM-field was then swept for optimized triangle apex size, gap and material. The electric field distribution (Re) sweep on the nanobowties with different gap size at lattice diffraction mode, fundamental mode and higher order mode (**Figure S2c**) confirmed the enhanced EM-field from the nanobowties with gap size of 15 nm under white light.

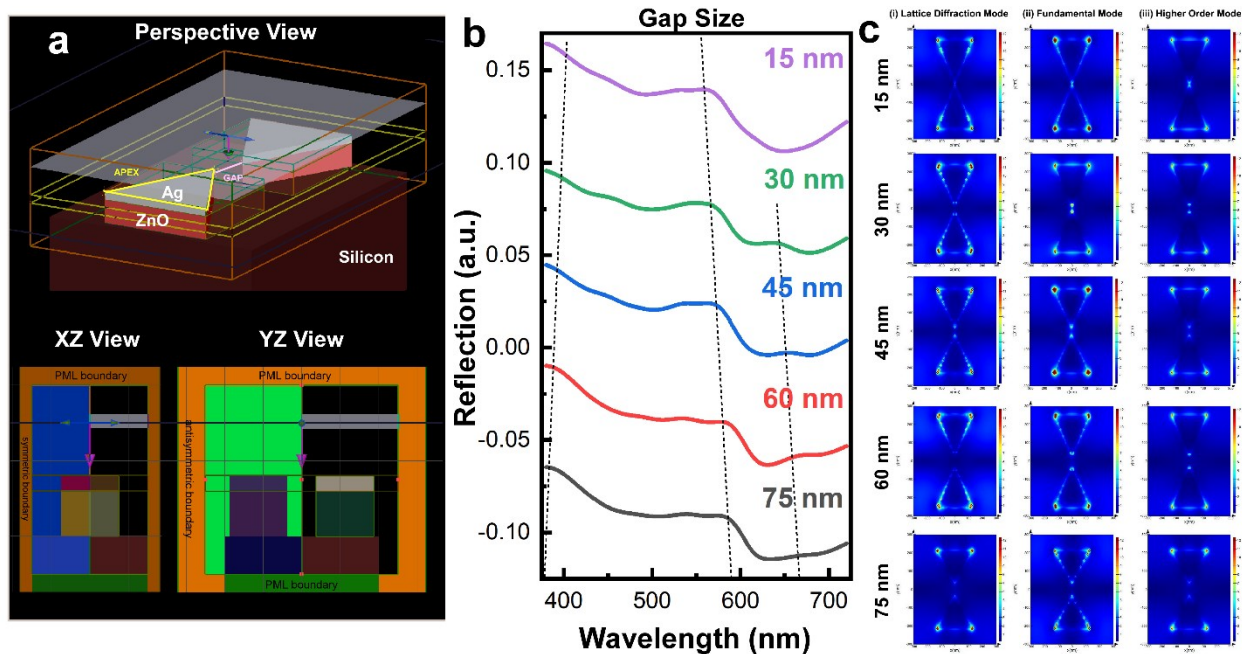


Figure S2. (a) The FDTD sketch of the nanobowtie pattern. (b) Simulated Reflectance spectra of plasmonic nanobowties using plane wave with different gap size. (c) The electric field distribution (Re) on the nanobowties with different gap size.

A TFSF source was used to simulate only a small region of the periodic structure, in order to find the maximally possible EM-field. The electromagnetic field enhancement factor E_{FEF} , which is an essential part to enhance SERS signal, scales with the 4th power of the electric field enhancement $E(\omega)/E_0(\omega)$ according to eq. S1:

$$E_{FEF} = \left(\frac{|E(\omega)|}{|E_0(\omega)|} \right)^4 \quad (\text{eq. S1})$$

As shown in the contour plots, the polarization mode can heavily affect the EFEF and place of the local field enhancement. **Figure S3a** shows the FDTD simulation of absorption spectra of the nanobowties with different distribution of gap-size using a total-field scattered-field (TFSF) light source. All broad-band absorbance spectra showed three defined absorption peaks between 450- 650 nm correlated to the diffraction mode. FDTD simulations of the maximum electric field enhancement as a function of the triangle size, defined by its apex length, are shown in supporting **Figure S3b**, while, FDTD simulations of the maximum electric field enhancement as a function of the varying apex gap, are shown in supporting **Figure S3c**.

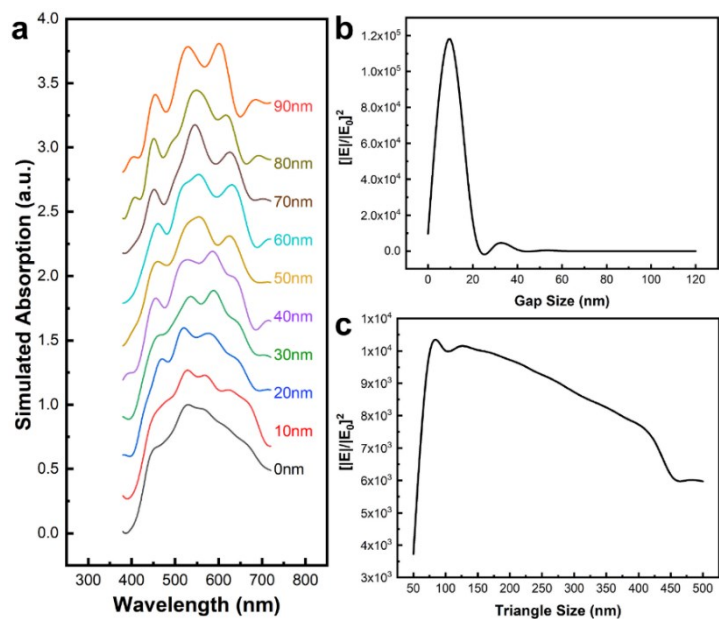


Figure S3. (a) Simulated absorption spectra of plasmonic nanobowties using TSFS wave centered at 532 nm with different gap size. (b) variation of $\sqrt{E_{FEF}}$ versus bowtie size (triangle width) (b) variation of $\sqrt{E_{FEF}}$ versus bowtie apex gap.

The EM-field intensity in a plasmonic nanoantenna is a function of the geometry and quality factor. A general equation to describe this field intensity for all plasmonic structures is unattainable. Therefore, a semiquantitative approach is used in the present study to describe the bowtie nanoantenna effect. For a bowtie, the field intensity is inversely proportional to the effective volume. For a small gap size, the field is highly confined in the gap region and the radiation loss is neglected for simplicity in analyses because the field is highly confined at the resonant frequency. While the effective volume of the bowtie gap cavity with fixed height is proportional to the product of the apex size (w), the gap size (g), the EM-field enhancement is proportional to $(wg)^{-1}$ (Figure S4)¹⁰.

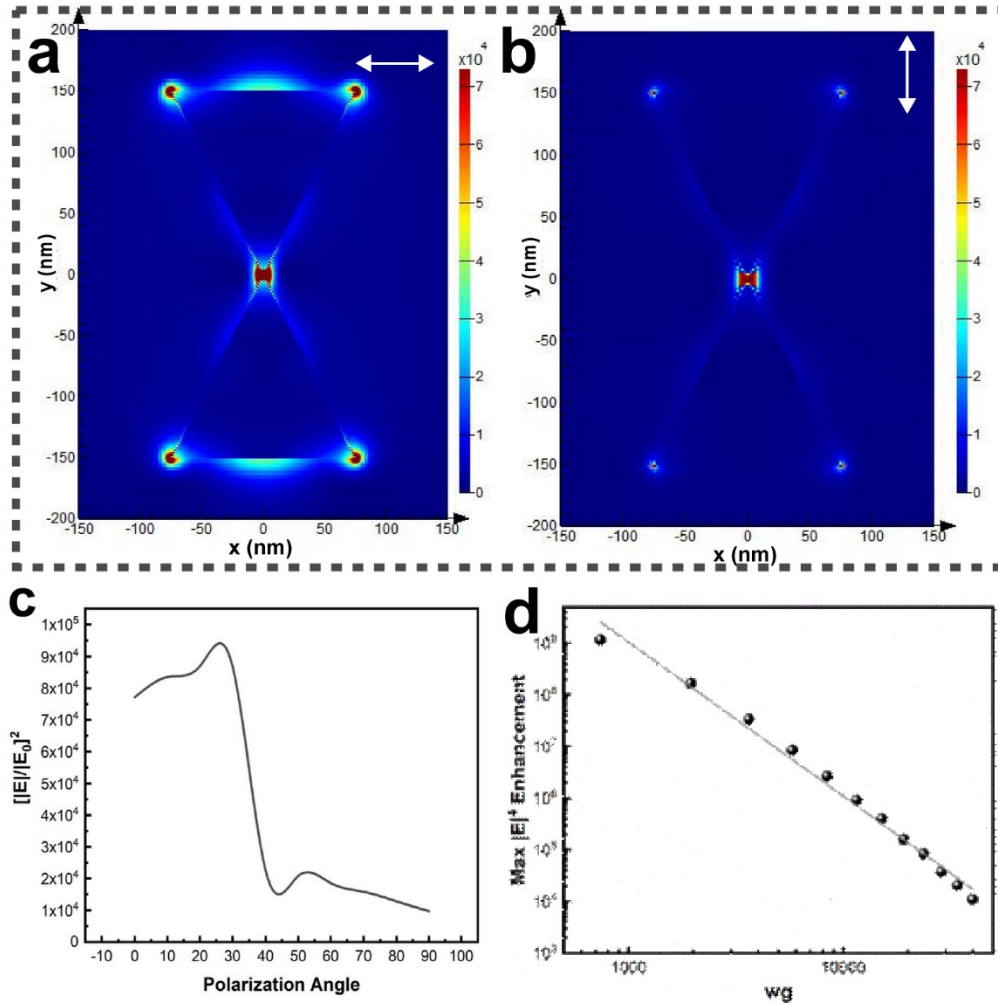


Figure S4. The maximum electric field distribution on nanobowties with gap size of 10 nm in (a) TE and (b) TM modes. (c) The variation of EM-field depending on the light polarization angle in a nanobowtie with 10 nm gap size. The maximum field enhancement $|E|^4$ calculated by FDTD as a function of the product of the apex width and the gap size, wg .

Concentration:

The SERS intensity (I_{SERS}) is directly proportional to the concentration of EVs according to¹¹:

$$I_{\text{SERS}} = F_s \sigma_s C_{\text{SERS}} \text{EFEF} \quad (\text{eq. S2})$$

where F_s is an instrumental factor related to Renishaw micro-Raman, σ_s is the Raman cross section of a particular analyte, and C_{SERS} is the concentration of the test analyte. When EFEF is optimized the I_{SERS} is directly proportional to C_{SERS} . According to **eq. S2** increasing the concentration of the small particulate

analyte (in this case EVs) enhances the I_{SERS} while overpopulating the substrate can hinder interaction of the analyte with plasmonic nanobowtie surface.

Figure S5a shows the SEM image representative of EVs from different fractions collected from purifying columns. A mixture of 7th to 10th fractions were used to study the EVs SERS fingerprint in this study. The size distribution decreases while going from lower fractions (i.e. 7th) to higher fractions (i.e. 10th), rendering an average size distribution of 157 ± 3.1 nm over the purified EVs mixture (detected by nanoparticle tracking analysis). The inset SEM image shows a low-resolution micrograph of accumulated EVs at 10^9 /ml concentration. **Figure S5b** shows representative SERS spectra of U373 EVs at different concentrations demonstrating that maintaining the concentrations at 10^8 /ml results in achieving more informative signals. **Figure S5c** shows the energy dispersion spectroscopy (EDS) of the surface demonstrating existence of carbon, nitrogen and phosphorus components illustrating the organic origin of the features.

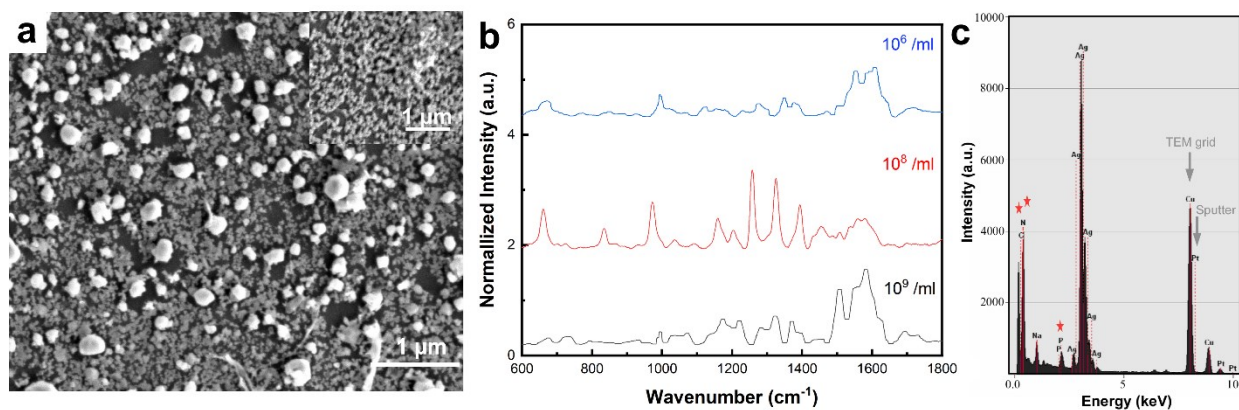


Figure S5. (a) Representative SEM image of EVs. Inset shows low resolution image of agglomeration with 10^9 /ml concentration. (b) representative SERS spectra of U373 EVs at different concentrations. (c) the EDS characterization of the surface.

COMSOL Simulation:

COMSOL Multiphysics is used to analyse the fluid flow in the microfluidic channel. Due to the creeping motion in microfluidic devices, laminar flow was defined in the simulation settings. The mesh independency of results is evaluated in the settings, based on which the fluid flow inside the channel is investigated. In addition, the effect of bowtie structure on fluid flow and the correlated streamlines is

studied. This study demonstrated a pressure drop in the microfluidic device along the centre line of bowtie structures.

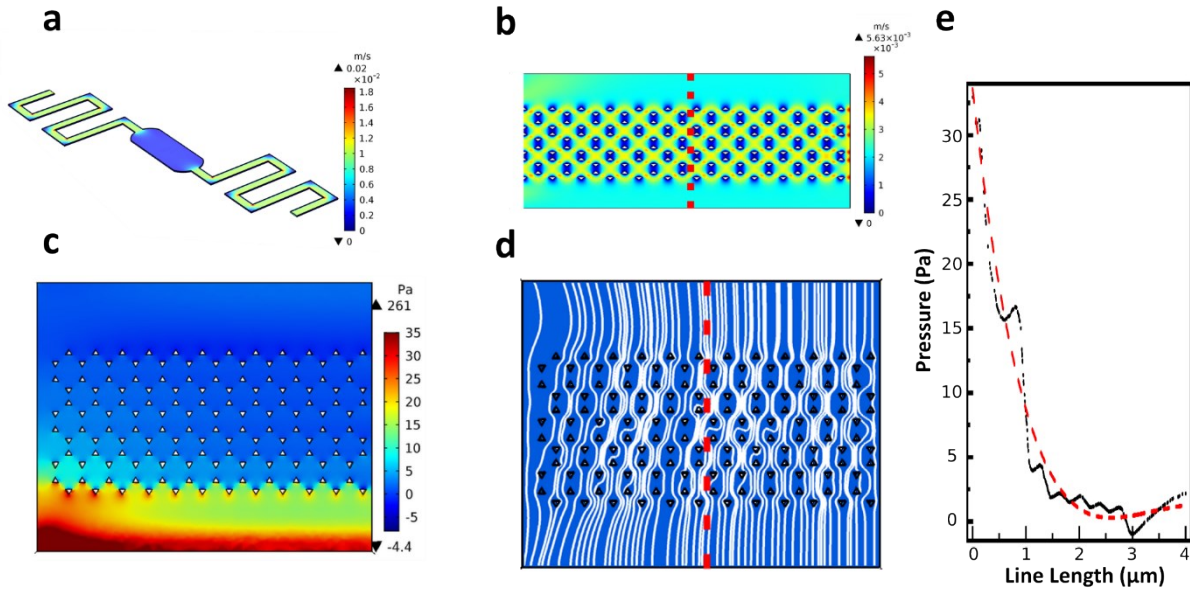


Figure S6. COMSOL simulation a) 3D simulation showing velocity distribution through the microfluidic device note lower flow velocities at the fluidic chamber to facilitate EV detection. b) 2D flow velocity in the plan of the Nanobowties. The simulation shows the velocity gradient in a $4 \mu\text{m} \times 10 \mu\text{m}$ section of the fluidic chamber. c) 2D pressure distribution plot for a $4 \mu\text{m} \times 5 \mu\text{m}$ section in the fluidic chamber. d) Streamlines (in white) representing the fluid flow paths around the Nanobowtie structures. e) line pressure distribution (red line in d) through an array of 3×11 nanobowtie structures as expected a pressure drop is observed through the length of the line. The pressure drop through the section is fitted by a polynomial fit shown by dotted red fit.

Brownian Dynamic Simulation:

Based on Faxén law¹², the drag force that particles sense in parallel of a surface is a function of the distance of the particle from the surface:

$$\gamma_{\parallel} = \frac{\gamma_0}{1 - \frac{9R}{16h} + \frac{R^3}{8h^3} - \frac{45R^4}{256h^4} - \frac{R^5}{16h^5}} \quad (\text{eq. S3})$$

In which, $\gamma_0 = 6\pi\mu R$ is the bulk drag coefficient ($y \rightarrow \infty$) when the viscosity of the fluid is μ (considered as $8.90e^{-4}$) and the radius of a particle is R while the axial drag force is.

$$\gamma_{\perp} = \frac{\gamma_0}{1 - \frac{9R}{8h} + \frac{R^3}{2h^3} - \frac{57R^4}{100h^4} + \frac{R^5}{5h^5} + \frac{7R^{11}}{200h^{11}} - \frac{R^{12}}{25h^{12}}}$$

(eq. S4)

The gradient of the drag coefficient leads to a higher number of particles near the surface and therefore keep the EVs in close proximity of the plasmonic surface. In **Figure S7**, the Brownian dynamic simulation of results is shown. The overdamped model of Langevin-Equation is used to analyze the Brownian motion of particles as follows: $\gamma V = \eta(t)$. $\eta(t)$ is thermal noise which is Gaussian distribution with correction function as: $\langle \eta_i(t) \eta_j(t) \rangle = 2\mu k_B T \delta_{i,j} \delta(t - t')$. k_B is Boltzman constant, T is the temperature (considered 298 K) and δ is a delta function. In the Langevin-Equation, the drag coefficient is updated based on the distance of particle (EVs) to the surface.

The size of the particles is chosen randomly based on NTA results. Particles are distributed homogenously in the channel. Our analysis shows that particles reach an equilibrium after 1 s (**Figure S7 a**). However, the data is collected after 10 seconds (9 seconds after equilibrium) to make sure that results represents the equilibrium condition. Here, we presented the data after 10 s to make sure that particles are in the final equilibrium. In **Figure S7 b** the Brownian motion of a particle along the y-axis is shown. As can be interpreted, the vibration of the particle is more restricted as much as it is closer to the surface. The probability distribution of particles along the y-axis is shown in **Figure S7 c** for 10^8 ml^{-1} concentration in a box with $2 \mu\text{m}$ height. The bar width is chosen based on the average particle size ($0.18 \mu\text{m}$). Particles are more concentrated near the surface and the probability of particles 1.5 time is more than the concentration of particles far from the surface. Our analysis shows that this distribution of particles in the box is independent of the concentration of particles. The bars in **Figure S7 c** show for different concentration (10^7 - 10^9 ml^{-1}). We can see that the probability distribution follows same value.

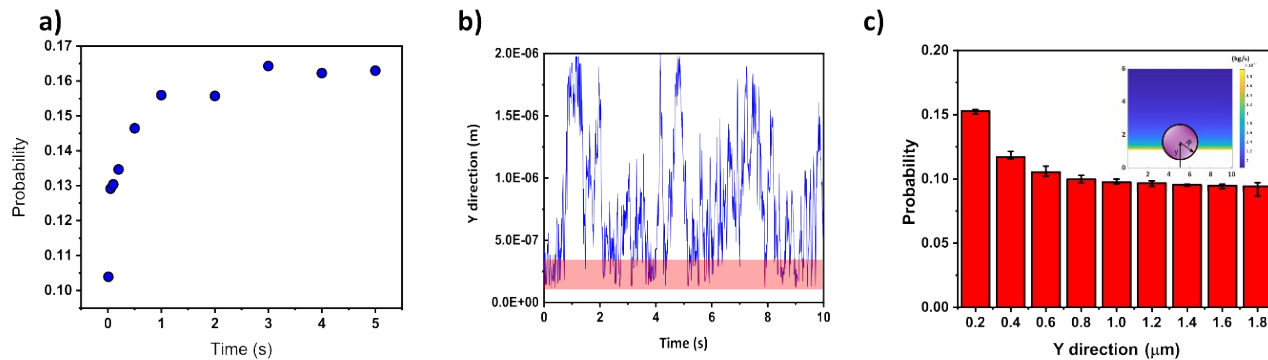


Figure S7. Brownian Dynamic simulation of EVs (a) the probability of particles for a box with $2\mu\text{m}$ height. (b) Brownian motion of EVs near the surface along the y-axis, (c) the probability of particles along for a box with $2\mu\text{m}$ height.

SERS:

Sensitivity- The sensitivity study of the NHA EVs in the range of 10^3 - 10^9 Particles ml^{-1} (**Figure S8a**) shows the SERS fingerprint peaks are detectable for concentrations over 10^6 ml^{-1} . The minimum concentration in which the SERS integrated band area at 1000 cm^{-1} (CH_2/CH_3 bending related to Phospholipid) is clearly defined is 10^5 Particles ml^{-1} (Inset). **Figure S8b** demonstrates the peak intensity variation at different relative wavenumbers. The intensity of the peaks increased similarly with the concentration of EVs from 10^3 - 10^9 Particles ml^{-1} leads to increment of the fingerprint peaks of the SERS spectra. The intensity fits with a sigmoidal growth function of $y=V_{\text{max}}*x^n/(k^n+x^n)$ with an average $R^2=0.985$ over the entire concentrations. The intensity augmentation shows a higher slope until 10^8 ml^{-1} concentration, while the slope starts to plateau when further increasing the concentration which could be due to the agglomeration of EVs and is in agreement with the physical simulations in Figure 4e-f. While a linear range is detected from 10^5 - 10^8 concentration demonstrating a limit of detection of 1.32×10^5 Particles ml^{-1} .

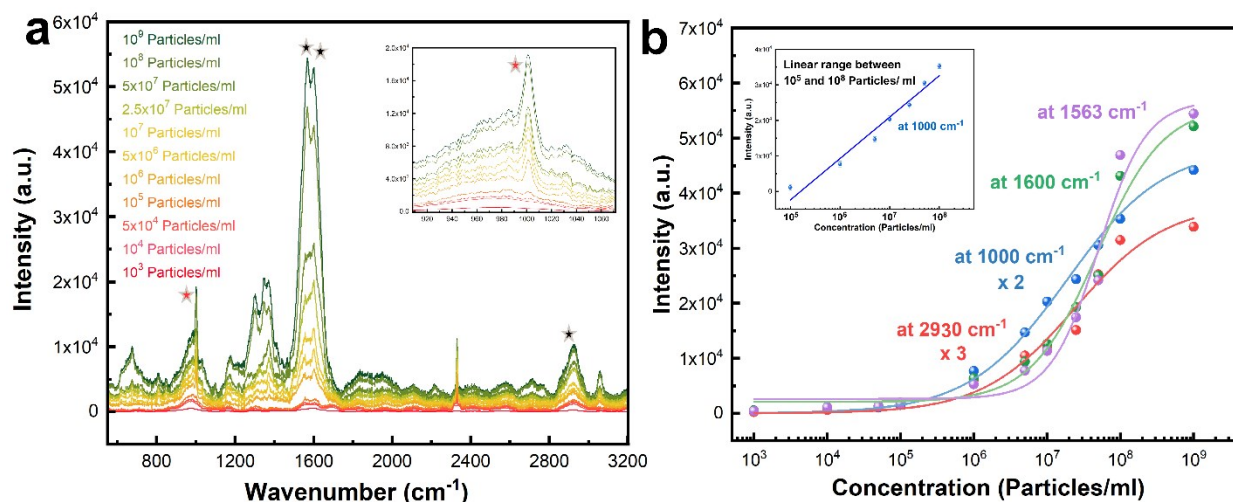


Figure S8. (a) The sensitivity study of NHA EVs demonstrating the fingerprint spectra of NHA EVs and the peak resolution variation with respect to the concentration of EVs. Inset: the intensity variation of the peak at 1000 cm^{-1} with respect to the concentration of the EVs. (b) The peak intensity variation at different relative wavenumbers fitted with a sigmoidal growth function in the concentration range of 10^3 - 10^9 particle ml^{-1} . Inset: shows the linear detection range of 10^5 - 10^8 .

Figure S9a presents unprocessed SERS spectra of 30 trials on U373 glioma EVs with plasmonic nanobowties. Unlike non-uniform metallic nanoparticle SERS substrates that mainly form a nonuniform plasmonic substrate, the signal analysis on nanobowties substrate (produced) a coherent EM field enhancement, therefore achieving encouraging reproducibility. The spectra are shifted vertically. Figure S9b shows the PCA analysis of the cancer U373 EVs, Liposomes and buffer (95% confidence ellipse). The first principal component (PC1), and second principal component (PC2) shown in Figure S9c, reveal the peaks responsible for similarity and differentiation between EVs and liposomes, respectively.

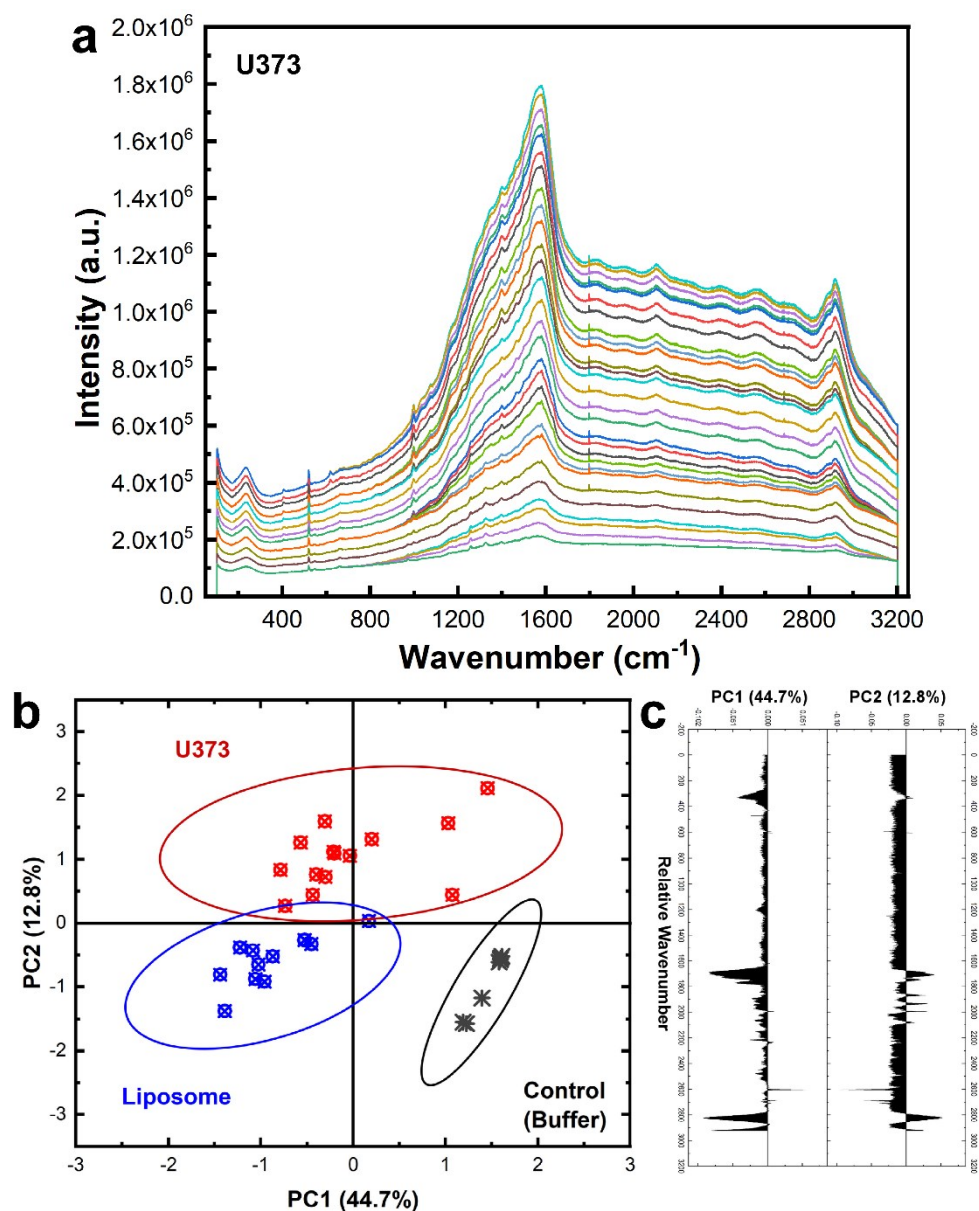


Figure S9. (a) Unprocessed SERS spectra of 30 trials on U373 glioma EVs with plasmonic nanobowties. (b) PCA score plot of the SERS data, demonstrating the distinguished position of the spectra from each sample according to (c) the shown PC1 and PC2 loading Raman bands.

To establish SERS efficiency of nanobowtie structures compared with silver thin film, it is necessary to compare the signals in similar conditions. The SERS integrated band area at 1000 cm^{-1} (CH_2/CH_3 bending related to Phospholipid) was chosen to perform the comparison. The integration boundaries were defined according to the average FWHM of the peak. The center was chosen to be

1000 cm^{-1} . The $\frac{\sum FWHM}{n}$ where, n is the number of trials, and FWHM is derived from the spectra of the

n trials shows the margin of the boundaries to be $1000 \text{ cm}^{-1} \pm 10$. The SERS signal from nanobowties at 1000 cm^{-1} is divided with that of the less enhanced Raman signal of the same band from silver thin film

(Figure S10) to calculate the $\frac{I_{SERS}}{I_{Flat}}$.

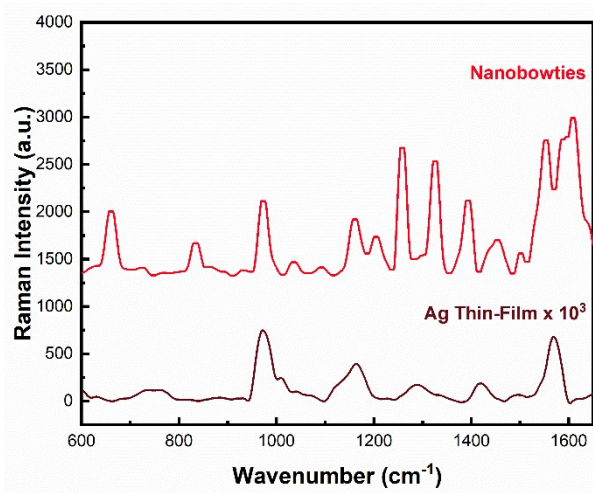


Figure S10. the intensity difference of the nanobowtie SERS spectra and Flat Ag thin film, from which $\frac{I_{SERS}}{I_{Flat}} = 1.3 \times 10^5$ was calculated at 1000 cm^{-1} .

Nanobowite plasmonic surface enhances quantitative EV fluorescence impacting:

To further investigate the EVs population, a fluorescent microscopy technique was studied on various substrates. The fluorescent micrograph of EVs loaded on glass (a), Si (b), Ag thin film (c), and nanobowtie structures (d) are shown in **Figure S11 (a-d)**. The initial concentration of test samples was fixed at $10^6/\text{ml}$. Plasmonic behaviour of Ag thin film and nanobowtie structures lead to surface enhanced fluorescent microscopy of ultra-small structures such as EVs. In particular, localized surface plasmon resonance (LSPR) behaviour of nanobowtie structures, leads to high sensitivity to the changes of effective refractive index of the surrounding media. The normal fluorescent microscopy of organic dyes is based on irradiation of the media via a single wavelength temporally coherent laser beam which is absorbed by the fluorophore and re-emitted in a different wavelength. There are several factors that cause fluorescent signal fluctuations in fluorescent ultra-small analytes like EVs leading to have dark states in microscopy, including formation of triplet state, polarization effect, and photo-induced isomerization of the fluorophores. When using a LSPR substrate the LSP fields increase the excitation rate of the fluorophore molecules in their vicinity due to the coupling of light with the SPs, followed by re-emission to the second surface (fluorophores) and secondary absorption of light by fluorescent molecules.

Figure S11e shows the corresponding fluorescent intensity count of fluorescently labelled EVs. The inset shows the efficiency of fluorescent intensity profile based on estimated loading of EVs to be 5000 counts per 0.005 mm² microscope field of view. The initial labelling process, and bleaching effect are the main reasons for low efficiency of fluorescent microscopy for all substrates. However, considering that the loading EVs were from same aliquot, the change in the efficiency can be due to enhanced gain of the fluorophore molecules which as explained earlier could be resulted from enhanced plasmonic resonances. This visualization provided a visible understanding of how SP resonances assist secondary absorption of laser beam by the molecules where LSPR of nanobowtie structures provide 15 times enhanced gain. Similarly, it is predicted that nanobowtie structures enhance the molecular gain of the laser while SERS characterization.

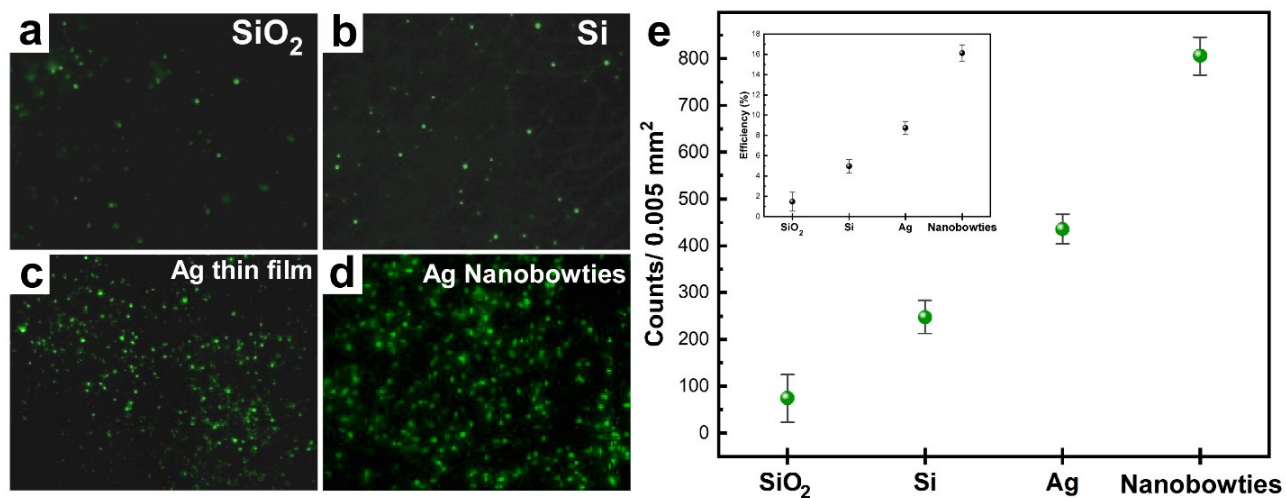


Figure S11. Fluorescence intensity profile of 10⁶ ml⁻¹ EVs on (a) glass, (b) Silicon, (c) Ag thin film, and (d) nanobowtie structures. (e) Comparison between the fluorescence intensity obtained from EVs on each substrate. Inset: Fluorescent microscopy efficiency calculated based on estimated 5000 EVs on 0.005 mm² area of microscope view.

The PCA analysis of EVs derived from two glioma cancer cells (i.e U373 and U87) shows distinguished the correlated 95% confidence ellipse of their fingerprints (**Figure S12**).

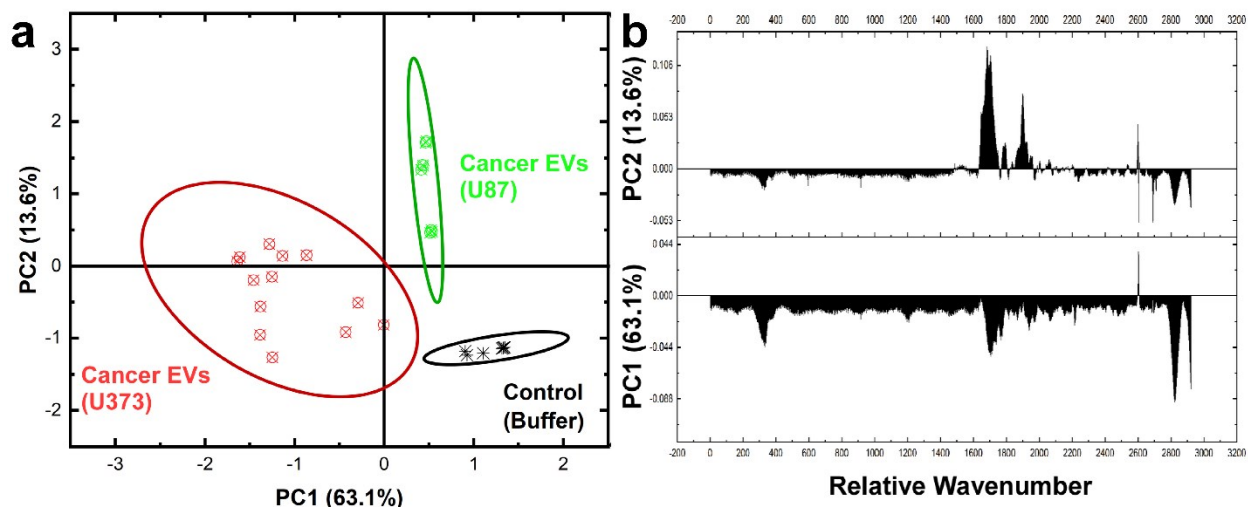


Figure S12. (a) SERS characterization for investigating the specific Raman scattering signals of EVs derived from glioma U87 EVs (Green) in comparison with glioma U373 EVs (Red). (b) PCA score plot of the SERS data, showing the distinguished position of the spectra of each sample according to the PC1 loading Raman bands.

References:

- 1 C. Lee, R. Carney, K. Lam and J. W. Chan, *J. Raman Spectrosc.*, 2017, **48**, 1771–1776.
- 2 Z. Weng, S. Zong, Y. Wang, N. Li, L. Li, J. Lu, Z. Wang, B. Chen and Y. Cui, *Nanoscale*, 2018, **10**, 9053–9062.
- 3 Y. Pang, C. Wang, L. Lu, C. Wang, Z. Sun and R. Xiao, *Biosens. Bioelectron.*, 2019, **130**, 204–213.
- 4 A. Knudson, S. Hazari, R. P. Carney, C. S. Robertson, K. S. Lam, S. Wachsmann-Hogiu, C. Lee and Z. J. Smith, *Nanoscale*, 2015, **7**, 9290–9297.
- 5 S. Zhu, H. Li, M. Yang and S. W. Pang, *Nanoscale*, 2018, **10**, 19927–19936.
- 6 F. Tantussi, G. C. Messina, R. Capozza, M. Dipalo, L. Lovato and F. De Angelis, *ACS Nano*, 2018, **12**, 4116–4122.
- 7 H. Im, H. Shao, Y. Il Park, V. M. Peterson, C. M. Castro, R. Weissleder and H. Lee, *Nat. Biotechnol.*, 2014, **32**, 490–495.
- 8 S. Stremersch, M. Marro, B. El Pinchasik, P. Baatsen, A. Hendrix, S. C. De Smedt, P. Loza-Alvarez, A. G. Skirtach, K. Raemdonck and K. Braeckmans, *Small*, 2016, **12**, 3292–3301.
- 9 H. Shin, H. Jeong, J. Park, S. Hong and Y. Choi, *ACS Sensors*, 2018, **3**, 2637–2643.
- 10 N. A. Hatab, C. H. Hsueh, A. L. Gaddis, S. T. Retterer, J. H. Li, G. Eres, Z. Zhang and B. Gu, *Nano Lett.*, 2010, **10**, 4952–4955.
- 11 J. C. Fraire, S. Stremersch, D. Bouckaert, T. Monteyne, T. De Beer, P. Wuytens, R. De Rycke, A. G. Skirtach, K. Raemdonck, S. De Smedt and K. Braeckmans, *ACS Appl. Mater. Interfaces*, 2019, **11**, 39424–39435.
- 12 H. Brenner, *Chem. Eng. Sci.*, 1961, **16**, 242–251.